

GP-GS: Gaussian Processes for Enhanced Gaussian Splatting

Zhihao Guo^{1,*} Jingxuan Su^{2,*} Shenglin Wang³ Jinlong Fan⁴ Jing Zhang⁵ Wei Zhou⁶
 Hadi Amirpour⁷ Yunlong Zhao⁸ Liangxiu Han¹ Peng Wang^{1,†}

¹ Manchester Metropolitan University

² SECE, Peking University

³ Pengcheng Laboratory

⁴ Hangzhou Dianzi University

⁵ Wuhan University

⁶ Cardiff University

⁷ University of Klagenfurt

⁸ Imperial College London

Abstract—3D Gaussian Splatting has emerged as an efficient photorealistic novel view synthesis method. However, its reliance on sparse Structure-from-Motion (SfM) point clouds often limits scene reconstruction quality. To address the limitation, this paper proposes a novel 3D reconstruction framework, Gaussian Processes enhanced Gaussian Splatting (GP-GS), in which a multi-output Gaussian Process model is developed to enable adaptive and uncertainty-guided densification of sparse SfM point clouds. Specifically, we propose a dynamic sampling and filtering pipeline that adaptively expands the SfM point clouds by leveraging GP-based predictions to infer new candidate points from the input 2D pixels and depth maps. The pipeline utilizes uncertainty estimates to guide the pruning of high-variance predictions, ensuring geometric consistency and enabling the generation of dense point clouds. These densified point clouds provide high-quality initial 3D Gaussians, enhancing reconstruction performance. Extensive experiments conducted on synthetic and real-world datasets across various scales validate the effectiveness and practicality of the proposed framework. The code is available at <https://github.com/zhihaohaoran/GPGS>.

I. INTRODUCTION

Novel View Synthesis (NVS) is a fundamental yet challenging problem in computer vision and computer graphics, aiming to generate novel viewpoints of a given scene from multi-view observations. It plays a critical role in applications such as digital twinning [29], virtual reality [9], [33], and robotics [27], [32]. Neural Radiance Fields (NeRF) [19] have revolutionized NVS by implicitly modelling volumetric scene representations, achieving high-fidelity rendering without explicit 3D geometry reconstruction. However, NeRF-based methods suffer from computational inefficiency and the requirement of dense sampling along rays, leading to slow inference speeds despite recent acceleration efforts [19], [23], [40].

To overcome these limitations, 3D Gaussian Splatting (3DGS) [13] and its variants [12], [17] have emerged as promising alternatives for real-time rendering. Unlike NeRF, which rely on ray-marching and volumetric integration, 3DGS represents scenes explicitly using a set of 3D Gaussians with learnable attributes like positions and colours. The rasterization-based splatting strategy can be considered a forward rendering

technique that avoids costly ray sampling and enables efficient parallel rendering, making it a compelling choice for NVS applications. However, existing 3DGS pipelines rely heavily on Structure-from-Motion (SfM) to extract 3D points by detecting and matching texture features like SIFT (Scale-Invariant Feature Transform) points, leading to sparse or incomplete point clouds, which is particularly the case in texture-less or clustered regions, respectively, leading to poor initialization of 3D Gaussians. Consequently, artefacts arise in the rendering process, causing a loss of fine details. To mitigate the limitations of sparse SfM-based reconstructions, the Adaptive Density Control (ADC) strategy has been introduced to 3DGS pipelines. ADC aims to improve scene coverage by dynamically duplicating Gaussians in underrepresented regions and removing redundant ones in over-reconstructed areas. However, ADC operates without explicit geometric priors, often producing noisy distributions that fail to adhere to the underlying scene structure. As a result, this leads to blurry reconstructions and poor occlusion handling, limiting the overall fidelity of 3DGS-based NVS. These challenges significantly limit the fidelity and robustness of 3DGS-based NVS methods, motivating the community for a more structured and adaptive approach to point cloud refinement and rendering.

In this paper, we propose GP-GS (Gaussian Processes for Enhanced 3D Gaussian Splatting), a novel framework designed to enhance the initialization of 3D Gaussians and improve rendered quality, especially in complex regions with densely packed objects (e.g., foliage) or under challenging lighting conditions. At the core of GP-GS is a Multi-Output Gaussian Process (MOGP) model that enables adaptive, uncertainty-guided densification of sparse point clouds generated by Structure-from-Motion (SfM). We formulate this task as a continuous regression problem, where the MOGP learns a mapping from 2D image pixels and their associated depth priors to a denser point cloud enriched with 3D position and color information. To ensure a structured and robust densification process, we propose an adaptive neighbourhood-based sampling strategy, where pixels are selected as candidate MOGP inputs for densification. For each sampled pixel, we predict its corresponding 3D point cloud attributes (position, colour, variance) using the MOGP model. To further refine

*Co-first author.

†Corresponding author.

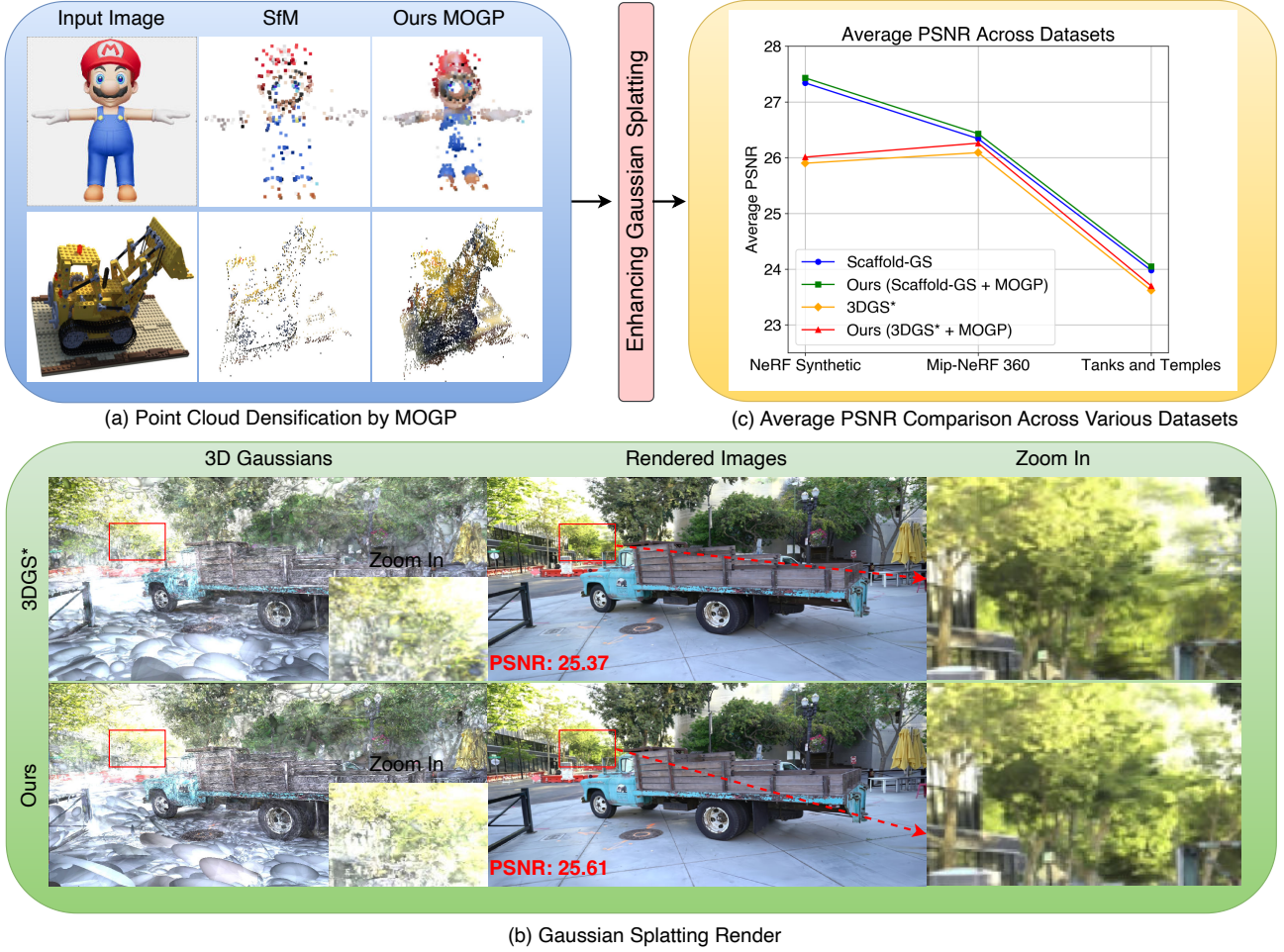


Fig. 1: Illustration of our MOGP-based enhancement for 3D Gaussian Splatting. (a) Conventional SfM often yields sparse point clouds, which struggle to capture fine scene details. Our Multi-Output Gaussian Process model mitigates this by densifying the sparse point clouds across various datasets, achieving 71% accuracy in position and colour prediction (as indicated by the R^2 score [7]) within the predicted confidence interval. (b) Compared to 3DGS* (official improvements), our approach (GP-GS) generates higher-fidelity renderings, particularly in challenging regions such as dense foliage and shaded areas. (c) Quantitative results across multiple datasets show that GP-GS achieves a 0.09 dB gain over 3DGS* and a 0.17 dB gain over Scaffold-GS on Mip-NeRF 360, and consistently outperforms baselines across all datasets.

the densified point cloud, we apply variance-based filtering to remove high-uncertainty predictions, reducing noise accumulation and preserving high-confidence reconstructions. The densified point clouds ultimately provide high-quality 3D Gaussian blobs (or Gaussians for brevity) to enhance the reconstruction performance.

Our **contributions** can be summarized as: 1) Gaussian Processes for Point Cloud Densityfication: We propose a MOGP model to densify sparse SfM point clouds by learning mappings from 2D image pixels and depth information to 3D positions and colours, with uncertainty awareness. 2) Adaptive Sampling and Uncertainty-Guided Filtering: We introduce an adaptive neighbourhood-based sampling strategy that generates candidate inputs for MOGP for 3D points prediction, followed by variance-based filtering to remove high uncertainty predictions, ensuring geometric consistency and enhancing rendering quality.

3) Our GP-GS framework can be seamlessly integrated into existing SfM-based pipelines, serving as a flexible plug-and-play module that improves the rendering quality of other NVS models.

II. RELATED WORK

A. Gaussian Processes

Gaussian Processes (GPs) are a collection of random variables, any finite number of which are subject to a joint Gaussian distribution [21]. GPs are particularly effective in handling sparse data, making them well-suited for scenarios with limited observations [25], [28]. Their flexibility and built-in uncertainty quantification enable robust predictions and uncertainty-informed signal processing, which has led to their widespread adoption in various computer vision tasks [24], [43].

Mathematically, a GP is fully specified by its mean function $m(\mathbf{x})$ and covariance function $k(\mathbf{x}, \mathbf{x}')$, a.k.a. kernel function, where \mathbf{x} and \mathbf{x}' are inputs. The kernel function typically depends on a set of hyperparameters θ , such as length scale l , signal variance σ_f^2 , or other parameters depending on the kernel type (e.g., Matérn). A GP is usually used as a prior over a latent function defined as:

$$f(\mathbf{x}) \sim \mathcal{GP}(m(\mathbf{x}), k(\mathbf{x}, \mathbf{x}')). \quad (1)$$

Training a GP model involves optimizing the hyperparameters θ of the kernel function to maximize the likelihood of the observed data. This is achieved by maximizing the log marginal likelihood, given by:

$$\log p(\mathbf{y} | \mathbf{X}, \theta) = -\frac{1}{2} \mathbf{y}^T \mathbf{K}^{-1} \mathbf{y} - \frac{1}{2} \log |\mathbf{K}| - \frac{n}{2} \log 2\pi, \quad (2)$$

where \mathbf{y} are the observed outputs, \mathbf{X} are the observed inputs, $\mathbf{K} \in \mathbb{R}^{n \times n}$ is the Gram matrix with entries computed using the kernel function $k(\mathbf{x}, \mathbf{x}')$ across all training inputs, and n is the number of training points. After training, the predictive distribution at a new test point \mathbf{x}_* follows a Gaussian distribution: $f(\mathbf{x}_*) | \mathbf{X}, \mathbf{y}, \mathbf{x}_* \sim \mathcal{N}(\mu_*, \sigma_*^2)$, where the predictive mean and variance are computed as:

$$\mu_* = \mathbf{k}_*^T \mathbf{K}^{-1} \mathbf{y}, \quad \sigma_*^2 = k(\mathbf{x}_*, \mathbf{x}_*) - \mathbf{k}_*^T \mathbf{K}^{-1} \mathbf{k}_*, \quad (3)$$

where $\mathbf{k}_* = [k(\mathbf{x}_*, \mathbf{x}_i)]^T, i = 1, \dots, n, \in \mathbb{R}^{n \times 1}$ represents the covariance between the test point \mathbf{x}_* and all training points, while $k(\mathbf{x}_*, \mathbf{x}_*)$ denotes the variance of the test point itself.

B. Neural Radiance Fields

NeRF [19] utilizes implicit representation for the first time to achieve photo-realistic perspective synthesis, subsequently inferring the 3D structure of the scene. It utilizes a limited number of input views to train a neural network to represent a continuous volumetric scene, enabling the generation of new perspectives of the scene once the neural network is trained. To be specific, given the 3D location $\mathbf{p} = [x, y, z]^T$ of a spatial sampling point (to be rendered) and 2D view direction $\mathbf{d} = [\theta, \phi]^T$ of the camera, NeRF predicts the color $\mathbf{c} = [r, g, b]^T$ of the sampling point and the volume density σ through a multi-layer perceptron (MLP) neural network [20] which can be represented as $F_\Theta : (\mathbf{p}, \mathbf{d}) \rightarrow (\mathbf{c}, \sigma)$, where F_Θ is the MLP parameterized by Θ . The color is estimated by volumetric rendering via quadrature, which can be formulated as

$$C(\mathbf{r}) = \int_{t_n}^{t_f} T(t) \sigma(\mathbf{r}(t)) \mathbf{c}(\mathbf{r}(t), \mathbf{d}) dt, \quad (4)$$

where $T(t) = \exp\left(-\int_{t_n}^t \sigma(\mathbf{r}(s)) ds\right)$, $C(\mathbf{r})$ is the sampling pixel color and is calculated by integrating the radiance value \mathbf{c} along the ray $\mathbf{r}(t) = \mathbf{o} + t\mathbf{d}$, in which \mathbf{o} is the camera position, \mathbf{d} is the direction from the camera to the sampled pixel, within near and far bounds t_n and t_f , and the function $T(t)$ denotes the accumulated transmittance along each ray from t_n to t . In cases where insufficient input images are used for training, the rendering quality of NeRF can be fairly poor [22]. Various enhancements have been proposed to improve NeRF's rendering quality. For instance, some works incorporate depth supervision

to enforce geometric constraints [10], [11], [31], [34], while others address challenges in low-light conditions [5], [26] and utilize a language model [16] to synthesize normal-light novel views and enhance the scene representation. However, the inherent inverse rendering approach in NeRF-based methods that necessitates dense sampling along each ray and represents the scene using an MLP is computationally intensive and presents challenges in optimization. Consequently, this hinders NeRF's applications in scenarios requiring rapid rendering or real-time performance.

C. 3D Gaussian Splatting

In contrast to NeRF's inverse rendering methodology, 3D Gaussian Splatting (3DGS) [13] employs a forward rendering approach. This technique represents scenes using 3D Gaussians and achieves efficient rendering by directly projecting these Gaussians onto the 2D image plane. By circumventing the need for extensive ray sampling and complex volumetric integration, 3DGS facilitates real-time, high-fidelity scene reconstruction. Specifically, it computes pixel colours by depth sorting and α -blending of the projected 2D Gaussians. This method avoids the complex calculation of ray marching and volume integration and can achieve real-time high-quality rendering and NVS. Several works have enhanced 3DGS, such as mitigating artifacts arising from camera pose sensitivity [38]. Others manage points to improve rendering quality [2], [18], [35], [42]. To the best of our knowledge, only a few studies have explored the densification of SfM point clouds for 3DGS performance improvement [3], [6]. To address this gap, we introduce a probabilistic model based on MOGP, which learns a continuous mapping from image pixels and depth priors to dense 3D point clouds with associated colour attributes. This approach not only improves reconstruction fidelity from sparse or dense SfM inputs but also provides principled uncertainty estimates, enabling adaptive pixel sampling and variance-based filtering for enhanced rendering and NVS.

While recent SfM-free methods such as HGM [4] and InstantSplat [8] achieve impressive results using pre-trained priors (e.g., MAST3R [15]) to initialize geometry and camera poses, they are highly dependent on the quality of learned priors and often require co-visibility filtering to reduce redundancy. In contrast, our method builds upon the widely used SfM pipeline, which offers a flexible, interpretable, and data-driven foundation without relying on large-scale pretrained models. Therefore, we focus our comparative analysis on SfM-based methods, aiming to improve this practical and widely adopted pipeline. We view SfM-free approaches as complementary but operating under different assumptions and problem settings.

III. PRELIMINARIES

3DGS [13] initialize SfM sparse point clouds as 3D Gaussians (ellipsoid shaped), each defined by specific parameters such as position (mean), rotation, scales, covariance, opacity α , and colour represented as spherical harmonics. For the sake of brevity, this paper abuses \mathbf{x} , representing the position of Gaussians, to define 3D Gaussian G as follows:

$$G(\mathbf{x}) = e^{-\frac{1}{2}(\mathbf{x}-\boldsymbol{\mu})^T \boldsymbol{\Sigma}^{-1}(\mathbf{x}-\boldsymbol{\mu})}, \quad (5)$$

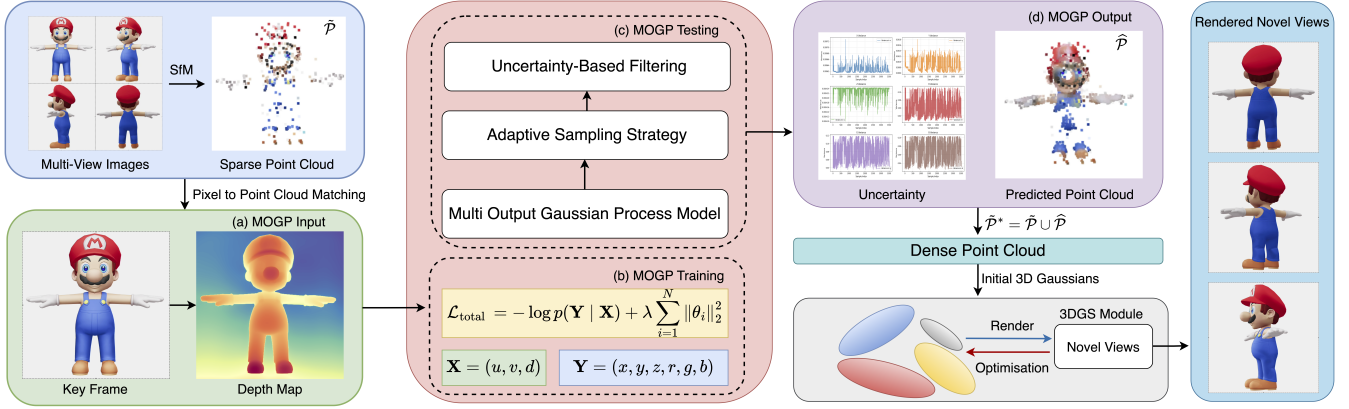


Fig. 2: **The overview of GP-GS.** (a) Key Frame and Depth Priors: Sparse point cloud is initially obtained using SfM. We then perform pixel-to-point cloud matching and select the key frame that contributes best to the point cloud. The selected key frame is processed with depth estimation models like Depth Anything [36] to extract the depth map. (b) Point Cloud Densification: MOGP is trained to take key frame pixel coordinates and depth as inputs $\mathbf{X} = [u, v, d]$ and predicts dense point clouds $\mathbf{Y} = [x, y, z, r, g, b]$ with uncertainty (variance). The loss function ensures an optimal mapping between input pixels and point clouds. (c) MOGP Testing: The adaptive sampling strategy adaptively generate sampling pixels within the image domain, and uncertainty-based filtering removes unreliable predictions. This results in a refined dense point cloud. (d) MOGP Output: The sparse and the predicted point clouds are merged and then used to initialize 3D Gaussians, which are then optimized to refine geometric details. The final rendered novel views demonstrate the effectiveness of GP-GS in reconstructing fine details while maintaining structural coherence.

where $\mu \in \mathbb{R}^{3 \times 1}$ is the mean vector, $\Sigma \in \mathbb{R}^{3 \times 3}$ is the covariance matrix. The 3D covariance Σ is a positive semi-definite matrix, which can be denoted as: $\Sigma = \mathbf{R}\mathbf{S}\mathbf{S}^T\mathbf{R}^T$, where $\mathbf{R} \in \mathbb{R}^{3 \times 3}$ is an orthogonal rotation matrix, and $\mathbf{S} \in \mathbb{R}^{3 \times 3}$ is a diagonal scale matrix.

3D Gaussians will be projected to 2D image space using the splatting-based rasterization technique. Specifically, the transformation is approximated with a first-order Taylor expansion at a projected point in the camera coordinate frame. This ensures efficient and accurate rendering from a given viewpoint. The 2D covariance matrix Σ' , which describes the elliptical shape of each Gaussian in the image space, is then computed as:

$$\Sigma' = \mathbf{J}\mathbf{W}\Sigma\mathbf{W}^T\mathbf{J}^T, \quad (6)$$

where \mathbf{J} is the Jacobian of the affine approximation of the projective transformation, and \mathbf{W} denotes the view transformation matrix [44]. The colour of each pixel is calculated by blending sorted Gaussians based on α , as follows:

$$c = \sum_{i=1}^n c_i \alpha_i \prod_{j=1}^{i-1} (1 - \alpha_j), \quad (7)$$

where n is the number of points, c_i is the color of the i -th point, α_i can be obtained by evaluating a projected 2D Gaussian with covariance Σ' multiplied with a learned opacity for each point.

IV. METHODOLOGY

A. Overview

This paper proposes a novel framework GP-GS that enhances 3D Gaussians initialization, thereby improving 3DGS rendering quality. The overview of GP-GS is presented in Figure 2. First,

addressing the limitations of sparse SfM point clouds, we propose the MOGP model to formulate point cloud densification as a regression problem. (Sec. IV-B). The training strategy of MOGP is introduced in Algorithm 1. Next, we adaptively densify sparse SfM point clouds and propose an uncertainty-based filtering strategy to remove high-uncertainty predictions. (Sec. IV-C).

B. Multi Output Gaussian Process

This section introduces MOGP to learn the relationship between pixels with depth priors and sparse SfM point clouds with position and colour information.

Problem Definition. We consider a MOGP regression problem, where the goal is to predict dense point clouds given image pixels and their corresponding depth priors. Given a set of n RGB images $\mathcal{I} = \{I_i\}_{i=1}^n$, we can extract the corresponding sparse point clouds $\mathcal{P} = \{\mathbf{P}_j\}_{j=1}^N$ with a total number of N points. Each point \mathbf{P}_j in the point clouds contains its 3D spatial position and the associated color information: $\mathbf{P}_j = [x_j, y_j, z_j, r_j, g_j, b_j]^T$, where $[x_j, y_j, z_j]^T$ are 3D coordinates and $[r_j, g_j, b_j]^T$ are RGB values.

Since a single 3D point can be visible from multiple views, it is straightforward to say that there can be multiple pixels from different images correspond to the same 3D point. Therefore, it is critical to learn the correspondences between 2D pixels and 3D points. To achieve this, we first perform pixel-to-point cloud matching to establish the correspondence between pixels and 3D points. This is done by projecting the sparse point clouds back to the image plane of each view and finding the corresponding pixel coordinates. The matching process can be formulated as:

$$\mathbf{P}_j = f(\mathbf{V}_{i_1}, \mathbf{V}_{i_2}, \dots, \mathbf{V}_{i_m}). \quad (8)$$

where \mathbf{V}_{i_k} are the pixels across different views $k = 1, \dots, m$ that project to the same point \mathbf{P}_j . Using f , we evaluate the contribution of RGB images $\mathcal{I} = \{I_i\}_{i=1}^n$ to point clouds $\mathcal{P} = \{\mathbf{P}_j\}_{j=1}^N$ based on the number pixel-to-point correspondences. The RGB image holds the most correspondences will be selected as the key frame for MOGP training.

To enhance densification performance, we leverage the key frame depth priors obtained from monocular depth estimation methods, such as [36]. These depth priors provide estimated depth values $\mathcal{D}_i(u_i, v_i)$ for each pixel with coordinate $[u_i, v_i]^T$. For brevity, we will use \mathcal{D}_i instead of $\mathcal{D}_i(u_i, v_i)$ below. The rationale behind choosing the monocular depth estimation method is that it strikes a trade-off between accuracy and efficiency, which will accelerate the overall performance of the GP-GS framework.

MOGP Formulation. Let the input features of the MOGP be denoted as $\mathbf{X}_i = [u_i, v_i, \mathcal{D}_i]^T \in \mathbb{R}^3$, where (u_i, v_i) are the pixel coordinates and \mathcal{D}_i is the associated depth value from a keyframe image. The corresponding output targets are $\mathbf{Y}_i = [x_i, y_i, z_i, r_i, g_i, b_i]^T \in \mathbb{R}^6$, representing the 3D spatial coordinates and RGB values. For notational convenience, we use $\mathbf{x} := \mathbf{X}_i \in \mathbb{R}^3$ and $\mathbf{y} := \mathbf{Y}_i \in \mathbb{R}^6$ to denote a single input-output pair.

We define a Multi-Output Gaussian Process (MOGP) over the function $\mathbf{y}(\cdot) : \mathbb{R}^3 \rightarrow \mathbb{R}^6$ as:

$$\mathbf{y}(\mathbf{x}) \sim \mathcal{GP}(\mathbf{m}(\mathbf{x}), \mathbf{K}(\mathbf{x}, \mathbf{x}')), \quad (9)$$

where the mean function $\mathbf{m}(\mathbf{x}) \in \mathbb{R}^6$ is defined as:

$$\mathbf{m}(\mathbf{x}) = \begin{bmatrix} m_1(\mathbf{x}) \\ m_2(\mathbf{x}) \\ \vdots \\ m_6(\mathbf{x}) \end{bmatrix}, \quad \text{with } m_j : \mathbb{R}^3 \rightarrow \mathbb{R}, \quad (10)$$

and the covariance function $\mathbf{K}(\mathbf{x}, \mathbf{x}') \in \mathbb{R}^{6 \times 6}$ is given by:

$$\mathbf{K}(\mathbf{x}, \mathbf{x}') = \begin{bmatrix} k_{11}(\mathbf{x}, \mathbf{x}') & \cdots & k_{16}(\mathbf{x}, \mathbf{x}') \\ \vdots & \ddots & \vdots \\ k_{61}(\mathbf{x}, \mathbf{x}') & \cdots & k_{66}(\mathbf{x}, \mathbf{x}') \end{bmatrix}, \quad (11)$$

with $k_{ij} : \mathbb{R}^3 \rightarrow \mathbb{R}$.

Loss Function and Optimization. For MOGP training, we employ a combined loss function that integrates negative log marginal likelihood and L2 regularization as shown in Equation (12). Such an optimization approach balances data likelihood maximization and regularization, leading to a more robust and generalizable MOGP model.

$$\mathcal{L}_{\text{total}} = -\log p(\mathbf{Y}|\mathbf{X}) + \lambda \|\boldsymbol{\theta}\|_2^2, \quad (12)$$

where $p(\mathbf{Y}|\mathbf{X})$ represents the marginal likelihood of the observed output given the inputs, $\lambda \|\boldsymbol{\theta}\|_2^2$ is the L2 regularization term, with $\lambda = 10^{-6}$ representing the weight decay. The L2 regularization helps prevent overfitting by penalizing large model parameters $\theta_i \in \boldsymbol{\theta}$, which are determined by the kernel.

To address the challenges posed by the sparse point clouds obtained through SfM, we employ a generalized Radial Basis

Function (RBF) kernel, specifically the Matérn kernel for training our MOGP model. In contrast to the standard RBF kernel, the Matérn kernel introduces a smoothness parameter ν , which governs the differentiability and local variations of the latent function, and ends up with a better trade-off between smoothness and computational efficiency. Formally, the Matérn kernel between two points \mathbf{x} and \mathbf{x}' is defined as:

$$k_\nu(\mathbf{x}, \mathbf{x}') = \sigma^2 \frac{2^{1-\nu}}{\Gamma(\nu)} (\sqrt{2\nu} \|\mathbf{x} - \mathbf{x}'\|)^\nu K_\nu(\sqrt{2\nu} \|\mathbf{x} - \mathbf{x}'\|), \quad (13)$$

where $\Gamma(\cdot)$ is the Gamma function, σ^2 is the variance, and $K_\nu(\cdot)$ is a modified Bessel function of the second kind. The parameter ν modulates how smooth the function can be: smaller ν values permit abrupt transitions, while larger ν values enforce smoother spatial changes. Details of tuning ν on various datasets can be found in Table II. Our MOGP training procedure can be found in Algorithm 1.

Algorithm 1 MOGP with Matérn Kernel

Input: RGB images \mathcal{I} , sparse 3D points \mathcal{P} , depth priors \mathcal{D} , pixel correspondences \mathcal{V} . Feature inputs $\mathbf{X} \in \mathbb{R}^{n \times 3}$, target outputs $\mathbf{Y} \in \mathbb{R}^{n \times 6}$.

Step 1: MOGP Definition

$$\mathbf{y} \sim \mathcal{MOGP}(\mathbf{m}(\mathbf{x}), \mathbf{K}(\mathbf{x}, \mathbf{x}')) \quad (14)$$

where $\mathbf{m}(\mathbf{x})$ is the mean function and $\mathbf{K}(\mathbf{x}, \mathbf{x}')$ is the covariance function.

Step 2: Matérn Kernel

$$k_\nu(\mathbf{x}, \mathbf{x}') = \sigma^2 \frac{2^{1-\nu}}{\Gamma(\nu)} (\sqrt{2\nu} \|\mathbf{x} - \mathbf{x}'\|)^\nu K_\nu(\sqrt{2\nu} \|\mathbf{x} - \mathbf{x}'\|) \quad (15)$$

where ν controls smoothness and σ^2 defines variance.

Step 3: Optimization Loss Function:

$$\mathcal{L}_{\text{total}} = -\log p(\mathbf{Y}|\mathbf{X}) + \lambda \|\boldsymbol{\theta}\|_2^2 \quad (16)$$

where $\lambda = 10^{-6}$ is the L2 regularization weight.

Gradient-Based Parameter Update:

- Initialize: $\boldsymbol{\theta} = [\sigma, \nu, \dots]^T$.
- for $t = 1 \dots T$:
 - Compute gradient $\nabla_{\boldsymbol{\theta}} \mathcal{L}_{\text{total}}$.
 - Update:

$$\boldsymbol{\theta} \leftarrow \boldsymbol{\theta} - \eta \nabla_{\boldsymbol{\theta}} \mathcal{L}_{\text{total}} \quad (17)$$

Output: Optimized GP hyperparameters $\boldsymbol{\theta}$. Predicted outputs $\hat{\mathbf{Y}}$ for new inputs $\hat{\mathbf{X}}$ via the MOGP posterior.

C. Point Cloud Densification

Point cloud densification involves an adaptive neighbourhood-based sampling strategy, which selectively identifies pixels as candidate inputs for the MOGP model (in section IV-B). The MOGP model subsequently predicts additional point clouds and applies uncertainty filtering to enhance the density.

Adaptive Sampling Strategy. To adaptively generate sampling pixels within the image domain, we introduce an adaptive neighbourhood-based sampling mechanism that samples from immediate circular neighbourhoods of each available training

point (u_i, v_i) . Specifically, we define a set of N sampled pixels $\tilde{\mathcal{P}}$ as follows:

$$\tilde{\mathcal{P}} = \bigcup_{i=1}^N \bigcup_{j=1}^M \left\{ \left(\frac{u_i + r \cos \theta_j}{W}, \frac{v_i + r \sin \theta_j}{H} \right) \mid (u_i, v_i) \in \mathcal{V}_i \right\}, \quad (18)$$

where $\theta_j \in [0, 2\pi)$ are uniformly distributed angles that control the sampling directions, $r = \beta \cdot \min(H, W)$ is the adaptive movement radius, $\beta \in (0, 1)$ controls the sampling scale, W and H denote the image width and height, respectively. W and H are used to normalize all samples to the range $[0, 1]$ in Equation (18). The parameter M determines the angular resolution of the sampling process. For each sampled pixel (u_i, v_i) , the corresponding depth value \mathcal{D}_i is retrieved from the depth image \mathcal{D} .

This adaptive procedure inherently controls spatial coherence by balancing the need for densification while avoiding redundant sampling. It selects regions near the training data to ensure that the test samples remain within the learned distribution of MOGP, mitigating extrapolation errors. Simultaneously, it prevents over-sampling by maintaining a distance between samples so that the generated points are not in the immediate proximity of existing Gaussians, thus avoiding their mergers within the adaptive density control framework of 3DGS.

Uncertainty-Based Filtering. The MOGP model then takes the sampled pixels $\tilde{\mathcal{P}}$ as inputs and provides inferred point clouds $\hat{\mathcal{P}}$ with uncertainty (variances). To identify and filter out low-quality predictions, we employ an empirical distribution of the average variances in the RGB channels, where we choose R^2 defined in Equation (20) as the quantile level, the details of which can be found in Table II. Let \hat{N} be the total number of inferred points in $\hat{\mathcal{P}}$, and $\Sigma \in \mathbb{R}^{\hat{N} \times 6}$ be the predicted variance, we compute the average variance over the RGB channels because it changes dramatically as shown in Figure 5, indicating high uncertainty. To refine the densified point clouds, we rank the average variances $\{\bar{\sigma}_i^2\}_{i=1}^{\hat{N}}$ in ascending order and determine the filtering threshold τ as $\tau = \bar{\sigma}_{\lceil R^2 \cdot \hat{N} \rceil}^2$, where R^2 is the variance quantile threshold and $\lceil \cdot \rceil$ denotes the ceiling function. Any point with an average variance exceeding τ is removed to maintain geometric consistency. Finally, the filtered densified point clouds $\tilde{\mathcal{P}}^*$ are formed by uniting the original training points with all inferred points: $\tilde{\mathcal{P}}^* = \mathcal{P} \cup \hat{\mathcal{P}}$.

An overview of the uncertainty-based filtering procedure can be found in Algorithm 2.

V. EXPERIMENTS

A. Dataset and Implementation Details

Dataset. Previous approaches to SfM often overlook the explicit correspondence between 2D image pixels and sparse 3D point clouds, we address this gap by introducing the Pixel-to-Point-Cloud dataset, which will be opensourced along the codes. This dataset provides a detailed mapping between image pixels and their corresponding 3D point clouds, thus facilitating more accurate modelling and enabling the training of our MOGP model. We further conduct a comprehensive evaluation

Algorithm 2 Dynamic Sampling and Filtering

Input: Image size (W, H) , depth map \mathcal{D} , training pixel coordinates $\{[u_i, v_i]^T\}_{i=1}^N$, angular resolution M , scale factor β , variance quantile threshold R^2 .

Step 1: Dynamic Sampling

- 1) Compute adaptive sampling radius $r = \beta \cdot \min(W, H)$.
- 2) **for** each training pixel with coordinates $[u_i, v_i]^T$:
 - Generate M new samples stacked as $[\mathbf{u}, \mathbf{v}]^T \in \mathbb{R}^{M \times 2}$ in a circular neighborhood.
 - Normalize $[\mathbf{u}, \mathbf{v}]^T$ and retrieve depth $\mathbf{d} \in \mathbb{R}^M$ from \mathcal{D} .
 - Store $[\mathbf{u}, \mathbf{v}, \mathbf{d}]^T$ in sample set $\tilde{\mathcal{P}}$.

Step 2: GP Inference Provide $\tilde{\mathcal{P}}$ to MOGP to infer a densified point cloud $\hat{\mathcal{P}}$ with variance matrix Σ .

Step 3: Variance-Based Filtering

- 1) Compute mean RGB variance $\bar{\sigma}^2$ for each inferred point.
- 2) Set threshold τ as the R^2 -quantile of the variance distribution.
- 3) Remove points with $\bar{\sigma}^2 > \tau$.

Step 4: Final Point Cloud $\tilde{\mathcal{P}}^* \leftarrow \mathcal{P} \cup \hat{\mathcal{P}}$.

Output: Densified and filtered point clouds $\tilde{\mathcal{P}}^*$.

of our method on dataset spanning NeRF Synthetic [19], Mip-NeRF 360 [1], and Tanks and Temples [14]. These benchmarks are popular in 3D reconstruction and novel-view synthesis due to their diverse characteristics, including high-fidelity 3D models, large-scale outdoor scenes with intricate scenes like clustered leaves, and lighting condition variations. By leveraging our new dataset and evaluation framework, we demonstrate the effectiveness of our approach in advancing point cloud densification and improving reconstruction fidelity across varied and challenging scenarios.

Implementation Details The MOGP-based densification process in GP-GS can be regarded as a plug-and-play module and can be integrated into any 3D reconstruction framework based on SfM sparse point clouds. We have integrated the process into 3DGS*, one of the state-of-the-art 3D reconstruction models, and compared their performance over the datasets mentioned earlier following 3DGS*'s training hyperparameters.

Our MOGP models are trained for 1,000 iterations across all scenes, we set L2 regularization weight $\lambda = 10^{-6}$, learning rate $l = 0.01$, dynamic sampling resolution $M = 8$, adaptive sampling radius $r = 0.25$. All experiments are conducted on an RTX 4080 GPU.

Metrics. The evaluation of the GP-GS is twofold, i.e., the evaluation of the SfM sparse point densification, and the evaluation of the novel view rendering performance. For densification, in line with prior studies on point cloud reconstruction and completion [37], [39], we adopt the mean Chamfer Distance (CD) to measure the discrepancy between the predicted point clouds and the ground truth. Specifically, for a predicted point set \mathcal{P} and its corresponding ground truth

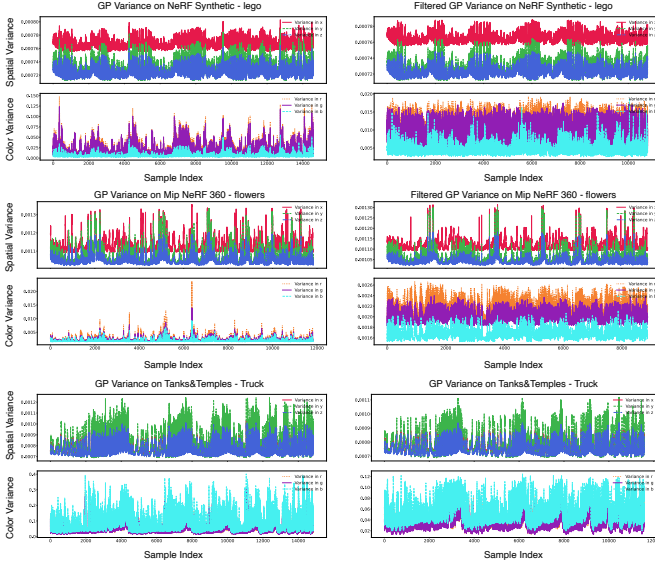


Fig. 3: Variance reduction comparison of our variance-based filtering Algorithm. The left and right columns display the variances before and after applying our filter. We can see that the variance in spatial components (x, y, z) and RGB channels (r, g, b) is significantly reduced, demonstrating the filter’s effectiveness in eliminating high-variance noise while preserving scene consistency and structural integrity.

set \mathcal{G} , the CD between them is calculated as:

$$d_{CD}(\mathcal{P}, \mathcal{G}) = \frac{1}{|\mathcal{P}|} \sum_{\mathbf{p}_i \in \mathcal{P}} \min_{\mathbf{g}_i \in \mathcal{G}} \|\mathbf{p}_i - \mathbf{g}_i\| + \frac{1}{|\mathcal{G}|} \sum_{\mathbf{g}_i \in \mathcal{G}} \min_{\mathbf{p}_i \in \mathcal{P}} \|\mathbf{g}_i - \mathbf{p}_i\|. \quad (19)$$

We also compute the Root Mean Squared Error (RMSE) and R^2 [7] to show the robustness of GP-GS under various metrics. The RMSE is calculated to quantify the average squared deviation between the predicted and true values, using $\text{RMSE} = \sqrt{\frac{1}{n} \sum_{i=1}^n (\mathbf{g}_i - \mathbf{p}_i)^2}$, a lower RMSE value indicates a more accurate prediction. The R^2 score captures the proportionate reduction in the residual variance:

$$R^2 = 1 - \frac{\sum_{i=1}^n (\mathbf{g}_i - \mathbf{p}_i)^2}{\sum_{i=1}^n (\mathbf{g}_i - \bar{\mathbf{g}})^2}, \quad (20)$$

where \mathbf{g}_i is the true value, \mathbf{p}_i is the predicted value, and $\bar{\mathbf{g}}$ is the mean of the true values. A higher R^2 (closer to 1) indicates better Gaussian process model performance.

For novel view rendering performance evaluation, we compare our method against state-of-the-art NVS approaches based on commonly used image-based metrics: Peak Signal-to-Noise Ratio (PSNR), Structural Similarity Index Measure (SSIM) [30], and Learned Perceptual Image Patch Similarity (LPIPS) [41] on the rendered images in the test views.

B. Results of Multi Output Gaussian Process

Quantitative Results To ensure the best performance of MOGP for densification, we evaluated MOGP model with

TABLE I: Comparison of different Matern kernel smoothness parameters ν . The best results are highlighted. **best R^2** , **best RMSE**, and **best CD**.

ν Value	$R^2 \uparrow$	RMSE \downarrow	CD \downarrow
0.5	0.71	0.13	0.21
1.5	0.67	0.15	0.24
2.5	0.61	0.14	0.26

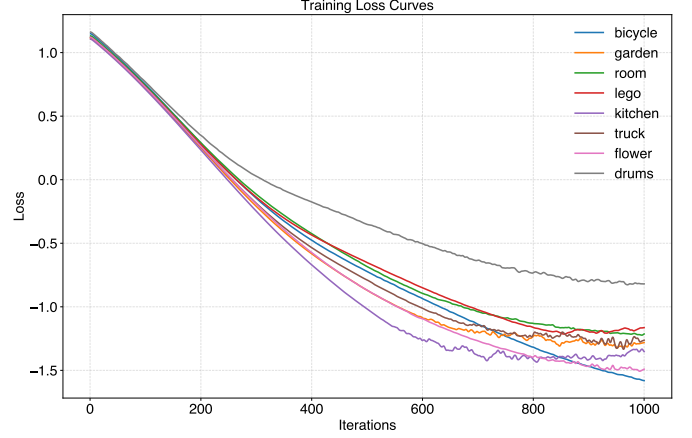


Fig. 4: MOGP training loss curves for different datasets over 1,000 iterations, the loss converges as training progresses.

different hyperparameters on our Pixel-to-Point-Cloud dataset, e.g., ν with values such as ($\nu \in \{0.5, 1.5, 2.5\}$). The data were split into an 80% training subset and a 20% testing subset, and the model was subsequently assessed using R^2 , RMSE, and CD as we mentioned in section V-A. The average outcomes of this analysis are summarized in Table I, which shows that $\nu = 0.5$ consistently yields the most favourable results. Consequently, we adopt $\nu = 0.5$ as our default configuration for subsequent experiments. Detailed metrics across multiple datasets for this kernel selection procedure are presented in Table II.

To validate the effectiveness of our variance-based filtering algorithm, we analyze the variance distributions across multiple Pixel-to-Point datasets, including NeRF Synthetic, Tanks & Temples, and Mip-NeRF 360, due to their diverse characteristics. The reduction in variance in all datasets suggests that our filtering method generalizes well to different types of 3D scenes, improving overall point cloud quality and enabling more accurate scene representation, as shown in Figure 3, the left column shows the spatial and colour variances before filtering on NeRF Synthetic (lego), Mip NeRF 360 (flowers) and Tanks & Temples (Truck), the right column presents the variances after applying our filter. The variances in spatial components (x, y, z) and colour channels (r, g, b) are significantly reduced, demonstrating that our filtering process effectively removes high-variance noisy points while preserving scene consistency.

MOGP Training Loss We also present the training loss curves of our MOGP model across different datasets. The loss curves illustrate the convergence behaviour of the model during training, providing insight into its stability and optimization progress. Figure 4 shows the loss curves for various datasets over 1,000 iterations, including bicycle, garden, room, lego,

TABLE II: Performance Metrics for MOGP Model Using Different Matern Kernel Parameters. The best results are highlighted. best R^2 , best RMSE, and best CD. We can see that $\nu = 0.5$ helps to produce the best densification results across various datasets.

Main Dataset	Sub Dataset	$\nu = 0.5$			$\nu = 1.5$			$\nu = 2.5$		
		$R^2 \uparrow$	RMSE \downarrow	CD \downarrow	$R^2 \uparrow$	RMSE \downarrow	CD \downarrow	$R^2 \uparrow$	RMSE \downarrow	CD \downarrow
NeRF Synthetic	Lego	0.78	0.12	0.18	0.75	0.13	0.20	0.69	0.15	0.21
	Chair	0.63	0.14	0.19	0.57	0.15	0.28	0.48	0.15	0.35
	Drums	0.52	0.22	0.61	0.52	0.22	0.64	0.52	0.22	0.64
	Hotdog	0.65	0.09	0.16	0.52	0.51	0.43	0.38	0.12	0.22
	Ficus	0.52	0.22	0.68	0.46	0.23	0.77	0.45	0.23	0.77
	Materials	0.53	0.19	0.24	0.49	0.20	0.24	0.48	0.20	0.39
	Ship	0.55	0.11	0.22	0.51	0.12	0.23	0.25	0.14	0.23
	Mic	0.45	0.23	0.69	0.42	0.23	0.70	0.43	0.23	0.71
	Average	0.58	0.17	0.13	0.53	0.22	0.44	0.46	0.18	0.44
Tanks & Temples	Truck	0.78	0.12	0.18	0.75	0.13	0.20	0.69	0.15	0.21
	Train	0.78	0.10	0.05	0.74	0.10	0.07	0.73	0.11	0.07
	Average	0.78	0.11	0.11	0.75	0.12	0.14	0.71	0.13	0.14
Mip-NeRF 360	Bicycle	0.74	0.10	0.12	0.70	0.11	0.12	0.47	0.16	0.41
	Bonsai	0.77	0.12	0.19	0.72	0.13	0.23	0.70	0.13	0.25
	Counter	0.85	0.10	0.13	0.82	0.11	0.13	0.82	0.11	0.14
	Garden	0.66	0.12	0.13	0.60	0.13	0.13	0.57	0.13	0.14
	Kitchen	0.82	0.08	0.05	0.79	0.08	0.06	0.79	0.09	0.08
	Room	0.74	0.097	0.136	0.71	0.104	0.143	0.68	0.109	0.156
	Flowers	0.75	0.115	0.15	0.72	0.122	0.214	0.69	0.125	0.152
	Average	0.77	0.10	0.13	0.72	0.11	0.15	0.67	0.12	0.19

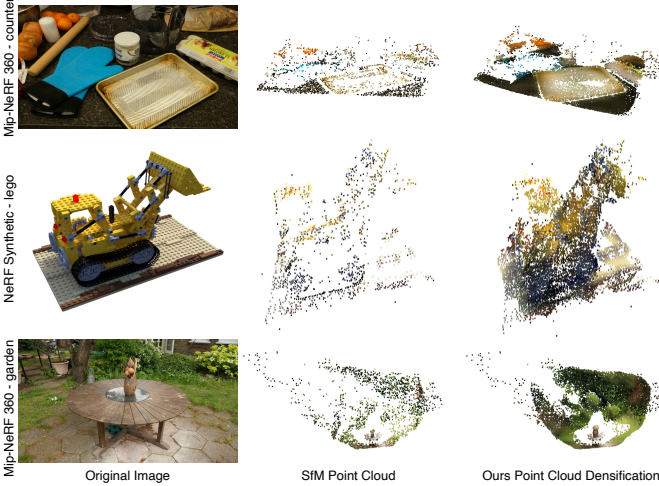


Fig. 5: Qualitative results comparison of our MOGP point cloud densification approach and SfM.

kitchen, truck, flower, and drums. Our MOGP model demonstrates a smooth and consistent decline in loss, indicating effective learning and convergence.

Qualitative Results Figure 5 presents the comparison of the original SfM sparse point clouds (middle) with our densified point clouds (right) for NeRF Synthetic (lego) (middle) and Mip-NeRF 360 (counter and garden) (top and bottom). The densified point clouds produced by our method significantly improve spatial completeness, effectively reducing gaps and enhancing fine detail preservation. Notably, the improvements are most pronounced in regions where the original SfM point clouds exhibit severe sparsity. For example, in the NeRF Synthetic - lego scene, our approach reconstructs the intricate structural components of the excavator more faithfully. Similarly, in Mip-

NeRF 360 - counter and garden, our method enhances surface continuity on the table while maintaining the overall geometric consistency of the scene. These qualitative results demonstrate the effectiveness of our approach in mitigating the limitations of sparse SfM reconstructions.

Further validating our densified point cloud, we present Figure 6, which shows 3D Gaussians during training. Our approach leads to more structured and coherent reconstructions, especially in complex regions with fine textures and occlusions. In the flower scene, our 3D Gaussian representation successfully reconstructs branches, trunks, and leaves on the left and right sides, while the original 3D Gaussian sphere remains blurry and lacks structural detail. Additionally, our method accurately preserves the flower shape in the middle, improving overall reconstruction fidelity. In the room scene, our method provides a clearer representation of the curtain folds on the left, whereas the original method produces irregularly shaped Gaussian spheres and visible artefacts. The highlighted insets further demonstrate that our method reduces visual artefacts and better preserves geometric consistency during training.

C. Quantitative and Qualitative Results on NVS

To evaluate the effectiveness and versatility of our MOGP method, we conduct comprehensive experiments on datasets Tanks & Temples, Mip-NeRF 360, and NeRF Synthetic. Our proposed MOGP model is designed to be plug-and-play, enabling seamless integration into existing novel view synthesis pipelines. We incorporate MOGP into both 3DGS* [13] and Scaffold-GS [18], and compare performance using both quantitative metrics and qualitative visualizations.

Quantitative Results Table III, IV, V report PSNR, SSIM, and LPIPS scores across all datasets, respectively. Our method consistently achieves higher PSNR and SSIM values

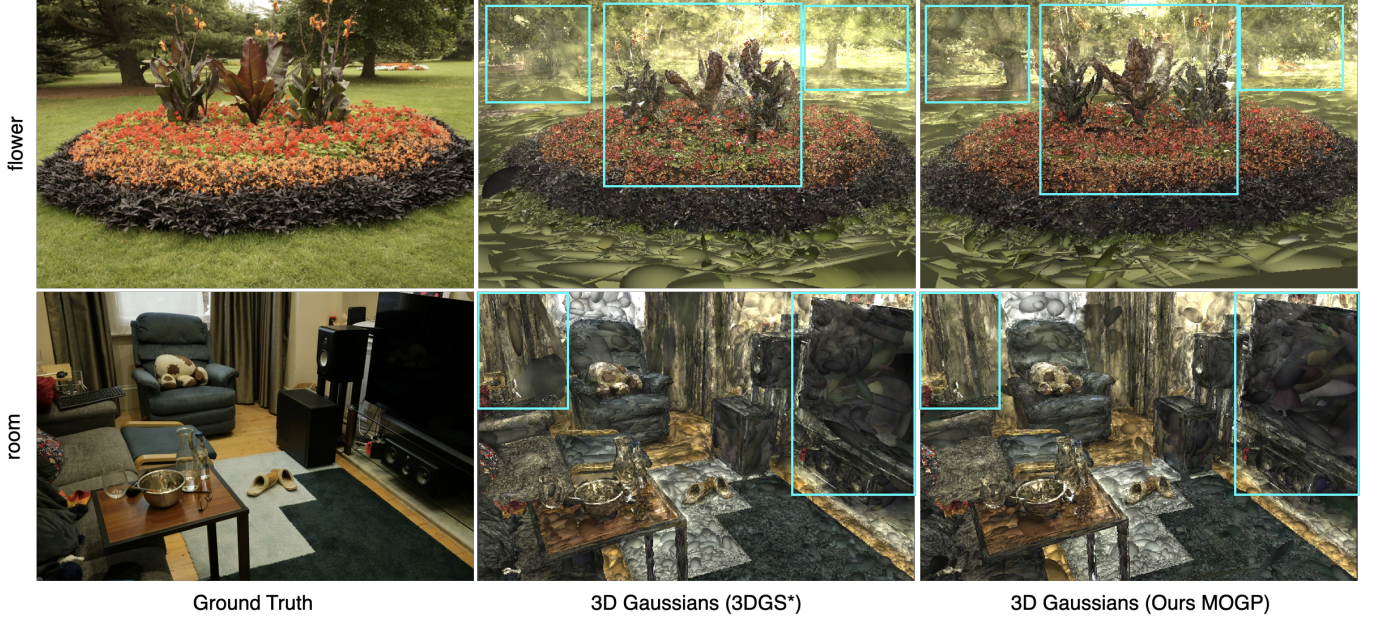


Fig. 6: Qualitative comparison of 3D Gaussians during 3DGS training process. The left column shows the ground truth images. The middle column presents 3D Gaussians from 3DGS*, while the right column shows 3D Gaussians generated using ours MOGP.

TABLE III: Comparison of Various Methods on Tanks and Temples. Best results are highlighted: **best PSNR**, **best SSIM**, and **lowest LPIPS**.

Dataset	Scaffold-GS			Ours (Scaffold-GS + MOGP)			3DGS*			Ours (3DGS* + MOGP)		
	PSNR \uparrow	SSIM \uparrow	LPIPS \downarrow	PSNR \uparrow	SSIM \uparrow	LPIPS \downarrow	PSNR \uparrow	SSIM \uparrow	LPIPS \downarrow	PSNR \uparrow	SSIM \uparrow	LPIPS \downarrow
Truck	25.45	0.879	0.150	25.57	0.880	0.150	25.10	0.876	0.153	25.18	0.877	0.153
Train	22.50	0.828	0.198	22.53	0.830	0.196	22.13	0.819	0.202	22.22	0.823	0.199
Average	23.98	0.854	0.174	24.05	0.856	0.173	23.62	0.847	0.178	23.70	0.850	0.176

TABLE IV: Comparison of Various Methods on NeRF Synthetic. Best results are highlighted: **best PSNR**, **best SSIM**, and **lowest LPIPS**.

Dataset	Scaffold-GS			Ours (Scaffold-GS + MOGP)			3DGS*			Ours (3DGS* + MOGP)		
	PSNR \uparrow	SSIM \uparrow	LPIPS \downarrow	PSNR \uparrow	SSIM \uparrow	LPIPS \downarrow	PSNR \uparrow	SSIM \uparrow	LPIPS \downarrow	PSNR \uparrow	SSIM \uparrow	LPIPS \downarrow
chair	30.89	0.976	0.027	30.92	0.976	0.027	30.99	0.978	0.024	30.99	0.978	0.024
drums	25.51	0.936	0.068	25.53	0.937	0.068	25.52	0.940	0.065	25.52	0.940	0.065
ficus	25.98	0.925	0.061	25.99	0.927	0.060	25.03	0.923	0.058	25.20	0.923	0.058
hotdog	34.51	0.978	0.042	34.61	0.978	0.041	34.53	0.979	0.037	34.55	0.979	0.037
lego	28.62	0.926	0.075	28.90	0.929	0.074	28.32	0.929	0.074	29.08	0.936	0.067
materials	17.88	0.749	0.221	18.11	0.755	0.219	16.82	0.734	0.239	16.68	0.736	0.241
mic	27.67	0.852	0.153	27.71	0.853	0.152	18.90	0.855	0.144	19.02	0.863	0.123
ship	27.66	0.853	0.153	27.65	0.852	0.151	27.08	0.848	0.157	27.05	0.849	0.154
Average	27.34	0.899	0.100	27.43	0.901	0.099	25.90	0.898	0.100	26.01	0.901	0.096

while maintaining lower LPIPS scores, indicating superior reconstruction quality and perceptual realism. The improvements are particularly evident in regions with high structural complexity and varying textures, such as dense foliage and intricate surfaces, where existing methods often suffer from over-smoothing and aliasing artefacts. Our approach effectively preserves fine details and enhances geometric consistency, even under challenging lighting conditions. Figure 7 provides a detailed visual comparison.

Qualitative Results As shown in Figure 7, we compare our method with 3DGS* on datasets Tanks & Temples (Truck),

Mip-NeRF 360 (Flowers and Bicycles), and NeRF Synthetic (Lego). Our GP-GS (right) outperforms 3DGS* (middle) in complex regions with densely packed objects (e.g., foliage) and challenging lighting conditions. Notably, in the flower scene, GP-GS reconstructs intricate structures like branches, trunks, and leaves more accurately, while 3DGS* produces blurry results. Similarly, in the truck and bicycle scenes, our method better preserves fine details, reducing artifacts and improving spatial consistency. These results further validate the effectiveness of GP-GS in enhancing 3D Gaussian splatting for reconstruction. Our method demonstrates superior performance



Fig. 7: Qualitative comparisons of novel view synthesis on three benchmark datasets: Tanks & Temples (Truck), Mip-NeRF 360 (flowers and bicycles), and NeRF Synthetic (lego). From left to right: Ground Truth, 3DGS*, Ours (MOGP + 3DGS*), Scaffold-GS, and Ours (MOGP + Scaffold-GS). This Figure highlight key differences in texture sharpness, structural coherence, and occlusion boundaries. Our method consistently recovers finer details (e.g., leaves, spokes, and edges) and preserves global geometry better across all scenes. These results further validate the effectiveness of our proposed plug-and-play MOGP module, which improves both 3DGS* and Scaffold-GS.

TABLE V: Comparison of Various Methods on Mip-NeRF 360. Best results are highlighted: best PSNR, best SSIM, and lowest LPIPS.

Dataset	Scaffold-GS			Ours (Scaffold-GS + MOGP)			3DGS*			Ours (3DGS* + MOGP)		
	PSNR↑	SSIM↑	LPIPS↓	PSNR↑	SSIM↑	LPIPS↓	PSNR↑	SSIM↑	LPIPS↓	PSNR↑	SSIM↑	LPIPS↓
bicycle	19.70	0.643	0.262	19.80	0.644	0.260	19.17	0.632	0.248	19.22	0.634	0.248
bonsai	18.25	0.588	0.445	18.50	0.593	0.437	18.66	0.579	0.458	18.69	0.581	0.455
counter	29.73	0.917	0.121	29.83	0.918	0.119	29.15	0.911	0.122	29.17	0.915	0.121
garden	29.56	0.919	0.064	29.53	0.919	0.064	29.10	0.915	0.063	29.38	0.920	0.061
kitchen	31.86	0.943	0.073	31.87	0.944	0.073	31.74	0.943	0.069	32.28	0.948	0.068
room	32.22	0.939	0.118	32.30	0.939	0.120	31.78	0.934	0.126	31.89	0.939	0.121
flowers	23.08	0.707	0.237	23.15	0.709	0.236	23.04	0.707	0.251	23.16	0.711	0.246
Average	26.34	0.808	0.189	26.43	0.809	0.187	26.09	0.803	0.191	26.26	0.807	0.189

in NVS by effectively reconstructing fine-grained details, reducing artifacts, and enhancing occlusion handling. The visual comparisons highlight key challenges in 3DGS* rendering, including occlusions, high-frequency textures (e.g., object edges and surface details), and lighting variations. Notably, the zoom-in regions (marked with red and blue boxes) illustrate our model's ability to recover fine structures more accurately than existing approaches. These results further validate the robustness of our method in handling complex scenes, offering improved perceptual quality and structural consistency across diverse datasets.

VI. CONCLUSION

We Propose GP-GS, a novel framework that enhances 3DGS and improves rendering quality by addressing the limitations of sparse SfM reconstructions. Our approach formulates point cloud densification as a continuous regression task using a Multi-Output Gaussian Process (MOGP), which adaptively densifies sparse SfM point clouds by learning mappings from 2D image pixels and depth priors to 3D positions and colors, guided by predictive uncertainty. Furthermore, we introduce an adaptive neighborhood-based sampling strategy to improve point cloud completeness while ensuring structured densification. To further refine the densified point clouds, we incorporate a variance-based filtering method, effectively removing high-uncertainty predictions and preserving geometric consistency. Extensive experiments on synthetic and real-world datasets show that GP-GS significantly improves 3D reconstruction quality, and can provide compact 3D Gaussian representation, especially in complex regions with densely packed objects or under challenging lighting conditions. Future work includes integrating temporal information for dynamic scenes and scaling to larger environments.

REFERENCES

- [1] Barron, J.T., Mildenhall, B., Verbin, D., Srinivasan, P.P., Hedman, P.: Mip-nerf 360: Unbounded anti-aliased neural radiance fields. In: Proceedings of the IEEE/CVF conference on computer vision and pattern recognition. pp. 5470–5479 (2022)
- [2] Bulò, S.R., Porzi, L., Kotschieder, P.: Revising densification in gaussian splatting. arXiv preprint arXiv:2404.06109 (2024)
- [3] Chan, K.C., Xiao, J., Goshu, H.L., Lam, K.M.: Point cloud densification for 3d gaussian splatting from sparse input views. In: Proceedings of the 32nd ACM International Conference on Multimedia. pp. 896–904 (2024)
- [4] Chen, J., Li, C., Zhang, J., Zhu, L., Huang, B., Chen, H., Lee, G.H.: Generalizable human gaussians from single-view image. arXiv preprint arXiv:2406.06050 (2024)
- [5] Chen, S., Yan, B., Sang, X., Chen, D., Wang, P., Guo, X., Zhong, C., Wan, H.: Bidirectional optical flow nerf: high accuracy and high quality under fewer views. In: Proceedings of the AAAI Conference on Artificial Intelligence. vol. 37, pp. 359–368 (2023)
- [6] Cheng, K., Long, X., Yang, K., Yao, Y., Yin, W., Ma, Y., Wang, W., Chen, X.: Gaussianpro: 3d gaussian splatting with progressive propagation. In: Forty-first International Conference on Machine Learning (2024)
- [7] Edwards, L.J., Muller, K.E., Wolfinger, R.D., Qaqish, B.F., Schabenberger, O.: An r^2 statistic for fixed effects in the linear mixed model. *Statistics in medicine* **27**(29), 6137–6157 (2008)
- [8] Fan, Z., Wen, K., Cong, W., Wang, K., Zhang, J., Ding, X., Xu, D., Ivanovic, B., Pavone, M., Pavlakos, G., et al.: Instantsplat: Sparse-view sfm-free gaussian splatting in seconds. arXiv preprint arXiv:2403.20309 (2024)
- [9] Fei, B., Xu, J., Zhang, R., Zhou, Q., Yang, W., He, Y.: 3d gaussian splatting as new era: A survey. *IEEE Transactions on Visualization and Computer Graphics* (2024)
- [10] Guo, S., Wang, Q., Gao, Y., Xie, R., Li, L., Zhu, F., Song, L.: Depth-guided robust point cloud fusion nerf for sparse input views. *IEEE Transactions on Circuits and Systems for Video Technology* (2024)
- [11] Guo, Z., Wang, P.: Depth priors in removal neural radiance fields. In: Annual Conference Towards Autonomous Robotic Systems. pp. 367–382. Springer (2024)
- [12] Guo, Z., Zhou, W., Li, L., Wang, M., Li, H.: Motion-aware 3d gaussian splatting for efficient dynamic scene reconstruction. *IEEE Transactions on Circuits and Systems for Video Technology* (2024)
- [13] Kerbl, B., Kopanas, G., Leimkühler, T., Drettakis, G.: 3d gaussian splatting for real-time radiance field rendering. *ACM Trans. Graph.* **42**(4), 139–1 (2023)
- [14] Knapitsch, A., Park, J., Zhou, Q.Y., Koltun, V.: Tanks and temples: Benchmarking large-scale scene reconstruction. *ACM Transactions on Graphics (ToG)* **36**(4), 1–13 (2017)
- [15] Leroy, V., Cabon, Y., Revaud, J.: Grounding image matching in 3d with mast3r. In: European Conference on Computer Vision. pp. 71–91. Springer (2024)
- [16] Liao, G., Zhou, K., Bao, Z., Liu, K., Li, Q.: Ov-nerf: Open-vocabulary neural radiance fields with vision and language foundation models for 3d semantic understanding. *IEEE Transactions on Circuits and Systems for Video Technology* (2024)
- [17] Liu, Z., Su, J., Cai, G., Chen, Y., Zeng, B., Wang, Z.: Georgs: Geometric regularization for real-time novel view synthesis from sparse inputs. *IEEE Transactions on Circuits and Systems for Video Technology* (2024)
- [18] Lu, T., Yu, M., Xu, L., Xiangli, Y., Wang, L., Lin, D., Dai, B.: Scaffold-gs: Structured 3d gaussians for view-adaptive rendering. In: Proceedings of the IEEE/CVF Conference on Computer Vision and Pattern Recognition. pp. 20654–20664 (2024)
- [19] Mildenhall, B., Srinivasan, P.P., Tancik, M., Barron, J.T., Ramamoorthi, R., Ng, R.: Nerf: Representing scenes as neural radiance fields for view synthesis. *Communications of the ACM* **65**(1), 99–106 (2021)
- [20] Popescu, M.C., Balas, V.E., Perescu-Popescu, L., Mastorakis, N.: Multilayer perceptron and neural networks. *WSEAS Transactions on Circuits and Systems* **8**(7), 579–588 (2009)
- [21] Rasmussen, C.E.: Gaussian processes in machine learning. In: Summer school on machine learning. pp. 63–71. Springer (2003)
- [22] Remondino, F., Karami, A., Yan, Z., Mazzacca, G., Rigon, S., Qin, R.: A critical analysis of nerf-based 3d reconstruction. *Remote Sensing* **15**(14), 3585 (2023)
- [23] Roessle, B., Barron, J.T., Mildenhall, B., Srinivasan, P.P., Nießner, M.: Dense depth priors for neural radiance fields from sparse input views. In: Proceedings of the IEEE/CVF Conference on Computer Vision and Pattern Recognition. pp. 12892–12901 (2022)
- [24] Su, J., Anderson, S., Mihaylova, L.: Holistic self-distillation with the squeeze and excitation network for fine-grained plant pathology classification. In: 2023 26th International Conference on Information Fusion (FUSION). pp. 1–7. IEEE (2023)
- [25] Su, J., Anderson, S., Mihaylova, L.S.: A deep learning method with cross dropout focal loss function for imbalanced semantic segmentation. In: 2022 Sensor Data Fusion: Trends, Solutions, Applications (SDF). pp. 1–6. IEEE (2022)
- [26] Wang, H., Xu, X., Xu, K., Lau, R.W.: Lighting up nerf via unsupervised decomposition and enhancement. In: Proceedings of the IEEE/CVF International Conference on Computer Vision. pp. 12632–12641 (2023)
- [27] Wang, P., Guo, Z., Sait, A.L., Pham, M.H.: Robot shape and location retention in video generation using diffusion models. In: 2024 IEEE/RSJ International Conference on Intelligent Robots and Systems (IROS). pp. 7375–7382. IEEE (2024)
- [28] Wang, P., Mihaylova, L., Munir, S., Chakraborty, R., Wang, J., Mayfield, M., Alam, K., Khokhar, M.F., Coca, D.: A computationally efficient symmetric diagonally dominant matrix projection-based gaussian process approach. *Signal Processing* **183**, 108034 (2021)
- [29] Wang, S., Zhang, J., Wang, P., Law, J., Calinescu, R., Mihaylova, L.: A deep learning-enhanced digital twin framework for improving safety and reliability in human-robot collaborative manufacturing. *Robotics and computer-integrated manufacturing* **85**, 102608 (2024)
- [30] Wang, Z., Bovik, A.C., Sheikh, H.R., Simoncelli, E.P.: Image quality assessment: from error visibility to structural similarity. *IEEE transactions on image processing* **13**(4), 600–612 (2004)
- [31] Wei, Y., Liu, S., Rao, Y., Zhao, W., Lu, J., Zhou, J.: Nerfingmvs: Guided optimization of neural radiance fields for indoor multi-view stereo. In: Proceedings of the IEEE/CVF International Conference on Computer Vision. pp. 5610–5619 (2021)
- [32] Yan, Z., Dong, W., Shao, Y., Lu, Y., Haiyang, L., Liu, J., Wang, H., Wang, Z., Wang, Y., Remondino, F., et al.: Renderworld: World model with self-supervised 3d label. arXiv preprint arXiv:2409.11356 (2024)

- [33] Yan, Z., Li, L., Shao, Y., Chen, S., Wu, Z., Hwang, J.N., Zhao, H., Remondino, F.: 3dsceneeditor: Controllable 3d scene editing with gaussian splatting. arXiv preprint arXiv:2412.01583 (2024)
- [34] Yan, Z., Padkan, N., Trybała, P., Farella, E.M., Remondino, F.: Learning-based 3d reconstruction methods for non-collaborative surfaces—a metrological evaluation. *Metrology* **5**(2), 20 (2025)
- [35] Yang, H., Zhang, C., Wang, W., Volino, M., Hilton, A., Zhang, L., Zhu, X.: Gaussian splatting with localized points management. arXiv preprint arXiv:2406.04251 (2024)
- [36] Yang, L., Kang, B., Huang, Z., Zhao, Z., Xu, X., Feng, J., Zhao, H.: Depth anything v2. arXiv preprint arXiv:2406.09414 (2024)
- [37] Yu, X., Rao, Y., Wang, Z., Liu, Z., Lu, J., Zhou, J.: PointR: Diverse point cloud completion with geometry-aware transformers. In: *Proceedings of the IEEE/CVF international conference on computer vision*. pp. 12498–12507 (2021)
- [38] Yu, Z., Chen, A., Huang, B., Sattler, T., Geiger, A.: Mip-splatting: Alias-free 3d gaussian splatting. In: *Proceedings of the IEEE/CVF Conference on Computer Vision and Pattern Recognition*. pp. 19447–19456 (2024)
- [39] Yuan, W., Khot, T., Held, D., Mertz, C., Hebert, M.: Pcn: Point completion network. In: *2018 international conference on 3D vision (3DV)*. pp. 728–737. IEEE (2018)
- [40] Zhang, K., Riegler, G., Snavely, N., Koltun, V.: Nerf++: Analyzing and improving neural radiance fields. arXiv preprint arXiv:2010.07492 (2020)
- [41] Zhang, R., Isola, P., Efros, A.A., Shechtman, E., Wang, O.: The unreasonable effectiveness of deep features as a perceptual metric. In: *Proceedings of the IEEE conference on computer vision and pattern recognition*. pp. 586–595 (2018)
- [42] Zhang, Z., Hu, W., Lao, Y., He, T., Zhao, H.: Pixel-gs: Density control with pixel-aware gradient for 3d gaussian splatting. arXiv preprint arXiv:2403.15530 (2024)
- [43] Zhu, Y., Wang, P., Mihaylova, L.: A convolutional neural network combined with a gaussian process for speed prediction in traffic networks. In: *2021 IEEE International Conference on Multisensor Fusion and Integration for Intelligent Systems (MFI)*. pp. 1–7. IEEE (2021)
- [44] Zwicker, M., Pfister, H., Van Baar, J., Gross, M.: Ewa volume splatting. In: *Proceedings Visualization, 2001. VIS'01*. pp. 29–538. IEEE (2001)